Research Article | Vol. 29, No. 26 / 20 Dec 2021 / Optics Express 42738
Optics EXPRESS

Phase imaging microscopy under the Gabor regime in a minimally modified regular bright-field microscope

VICENTE MICÓ,* KARINA TRINDADE, AND JOSÉ ÁNGEL PICAZO-BUENO

Departamento de Óptica y de Optometría y Ciencias de la Visión, Universidad de Valencia, C/ Doctor Moliner 50, Burjassot 46100, Spain
*vicente.mico@uv.es

Abstract: Quantitative phase imaging (QPI) is nowadays a powerful tool for visualization and analysis of biological processes. QPI is usually attained from specifically designed optical microscopes retrieving phase information in a quantitative way. In this paper we report on an extremely simple, low cost and compact way to update a standard bright-field microscope with coherent sensing capabilities. It is based on the in-line Gabor holography concept and only needs to replace the illumination broadband source of the regular microscope with a coherent one. The proposed methodology is completed by the recording of a digital in-line Gabor hologram instead of regular imaging conditions and by the numerical processing of the recorded hologram to finally achieve QPI. The selection of the defocus distance is critical to finally achieve high quality phase imaging, so calibration considering phase and amplitude test targets is presented for the proper definition of such defocus distance. In addition, the selected configuration is experimentally validated using different samples (microbeads, cheek cells and alive spermatozoa). All the experiments are implemented in a regular Olympus BX-60 upright microscope using a 20X 0.46NA objective lens. The proposed method shows how to convert a regular microscope into a holographic one with probably the minimum needed modifications and with the main limitation coming from the Gabor imaging conditions (weak diffractive samples and twin image presence).

1. Introduction

Digital holographic microscopy (DHM) is a well-known and versatile imaging modality in different areas of biological research [1–4] as well as for industrial applications [5–6]. In particular, DHM allows visualization of phase samples using a non-invasive (no need for stained samples), full-field (non-scanning), real-time (on-line control), non-contact (no sample damage) and static (no moving components) operating principle [7]. Because of its interferometric principle, DHM has been proposed using as basic layout all the different experimental arrangements proposed along the years for classical interferometry, that is, Mach-Zehnder [8,9], Michelson [10], Linnik [11], Mirau [12], Twyman-Green [13], Sagnac [14,15], Lloyd [16] and common-path interferometry [17–19].

Especially relevant are those DHM layouts based on non-complex arrangements because they provide compact and cost-effective solutions in an easy-to-use manner for quantitative phase imaging (QPI) [20–22]. In that sense, it is interesting to point out some DHM implementations using just one optical element to produce interferences such as a Lloyd's mirror [16], a thick glass plate [23], a prism [24], a diffraction grating [25,26], a beam splitter cube [27] or a Fresnel's biprism [28]. Some of them are based on sparse sample constraints [16,23] meaning that the sample is restricted to a limited area and the surrounded free space is used as reference beam. By contrast, other strategies leave a clear region at the input plane by field of view (FOV)

#444884 https://doi.org/10.1364/OE.444884
Journal © 2021 Received 1 Oct 2021; revised 13 Nov 2021; accepted 16 Nov 2021; published 8 Dec 2021

Optics EXPRESS

multiplexing [24–28] to transmit in parallel both object and reference beams through the imaging system. On both cases, the two beams are combined with different optical elements to produce the interferometric recording. Also following this plan of minimum complexity (at least from an experimental point of view) to allow QPI, there is another appealing strategy consisting in adapting an external module to the exit port of a conventional bright-field microscope to convert it into a microscope with coherent sensing capabilities. Some examples are modules based on wavefront sensing [29,30], Michelson-based layouts [31–33], lateral shearing interferometers [34–36], transport of intensity equation methodologies [37–39], diffraction phase microscopy [3], using a beam splitter interferometer [40] or with a purely numerical add-on module [41].

In this contribution, we present an extremely simple (probably the most), low cost (only the illumination source needs to be replaced) and compact (no modifications in the microscope embodiment) way to convert a standard bright-field microscope into a holographic one. It is based on in-line Gabor holography concept [42,43] where a coherent source illuminates the sample in transmission mode and the diffracted wavefront passes through a conventional microscope embodiment arriving to the digital sensor plane. In a standard imaging configuration, the sample plane becomes conjugated with the digital sensor plane. In that case, transparent samples are not imaged since they provide a tiny (theoretically null) variation of the light intensity field. But when the digital sensor is moved away from the conjugated imaging plane or the sample is axially displaced from the input object plane, a defocused image in the form of a diffraction pattern is recorded by the digital camera. Thus, assuming that the sample is a weak diffractive sample [44], the recorded defocused image can be considered as a digital Gabor in-line hologram where the magnification is not coming from the geometrical projection of the sample as in the lensless geometry but introduced by the microscope objective used in the layout. In this case, it is possible to numerically refocus to the best imaging plane using digital propagation algorithms [45] to visualize the sample under different imaging modalities including QPI, phase contrast and DIC, just to cite some examples.

Although there are some previously reported references using a similar concept (digital Gabor in-line configuration merged with a microscope layout), they are applied to three-dimensional (3D) tracking of particles [46–51] and to determine the best focus criterion in DHM [52–54]. This manuscript exploits the advantages provided by the holographic principle proposed by Gabor [42] as the simplest holographic layout ever implemented and adapts it to the field of DHM for QPI. Thus, it takes all the advantages provided by actual microscopes concerning image quality, compactness and stability with coherence sensing capabilities coming from digital in-line holographic microscopy. The paper is organized as follows. Section 2 provides a description of the experimental layout and presents its calibration for the definition of the best defocus distance considering both amplitude and phase resolution test targets. Section 3 includes the experimental validation for different types of samples (microbeads, cheek cells and live sperm cells). And finally, Section 4 concludes the paper.

2. System description and validation

2.1. Experimental layout and numerical processing

The concept underlaying the proposed approach can be easily visualized through Fig. 1, representing a regular upright microscope embodiment (Olympus BX-60 with UMPlanFl 20X 0.46NA objective) where a fiber coupled diode laser is externally inserted to provide coherent illumination in the system. We have used the blue laser light (450 nm) of the multiwavelength illumination source from Blue Sky Research (SpectraTec 4 STEC4 405/450/532/635 nm). Thus, under regular imaging conditions [left scheme at Fig. 1(a)], the microscope provides an output image of the input object just where the digital camera (Mightex USB3.0 SMN-B050-U, CMOS sensor type, 2560×1920 pixels, 2.2×2.2 μm pixel pitch) is placed. But to allow digital in-line Gabor holographic recording, either the camera or the object must be axially displaced from

Optics EXPRESS

its conventional position [right scheme at Fig. 1(a)]. From these two options, we have selected to shift the object by a double reason. First, the sample can be easily moved up or down in a microscope using the fine/coarse adjustment knob mechanism while the camera is fixed at the output port. Moreover, the shifted distance can be easily quantified by reading on the adjustment knob angular scale. And second, the displacement of the camera at the image space ($\Delta z'$) must be larger than the sample one at the object space (Δz) because of they are related through the square of the objective magnification being used in the form of $\Delta z' = -M^2 \Delta z$. Hence, this procedure can lead in a bulky and disproportionate apparatus for the case of moving the camera. For both reasons, we have decided to vertically shift the object position by a certain amount Δz.

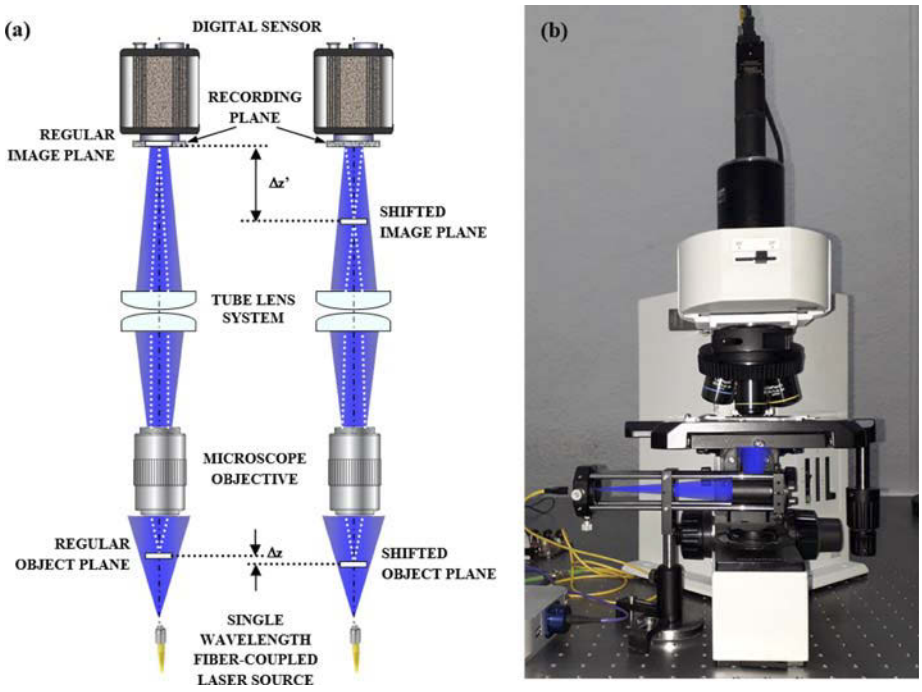

Fig. 1. Optical arrangement of the proposed approach: (a) scheme and (b) picture at the lab. The sample is shifted from its regular object plane position ($\Delta z > 0$ in the representation) allowing to shift the conjugated image plane ($\Delta z'$) and the digital recording of an in-line hologram. A right-angle mirror introduces the illumination beam in the microscope embodiment to provide more space for beam manipulation.

Nonetheless the distance Δz can be either negative or positive, meaning that the sample is moved closer or away to the microscope objective, respectively. Thus, the image plane considering $\Delta z < 0$ will fall behind the camera plane while it will be placed ahead the camera plane for $\Delta z > 0$. Note that a digital in-line Gabor hologram will be recorded by the camera on both cases. The selection of the best Δz distance is presented in next subsection and, by now, let's assume that no image of the object is recorded by the digital camera, so numerical refocusing needs to be applied to allow imaging conditions from the proposed experimental layout. Thus, the recorded hologram is digitally propagated using the convolution method applied to the diffraction Rayleigh-Sommerfeld integral [41] where the diffraction integral is numerically computed by using three Fourier transformations through the convolution theorem, that is:

$$U_0(x, y; d) = FT^{-1}\{FT\{U(x, y)\} \times FT\{h(x, y; d)\}\} \tag{1}$$

Optics EXPRESS

where $U_0(x,y;d)$ is the numerically propagated complex amplitude wave field at the object plane, $U(x,y)$ is the amplitude at the recording plane coming from the recorded intensity distribution (in-line Gabor hologram), $h(x,y;d)$ is the impulse response of free space propagation, (x,y) are the spatial coordinates, FT is the numerical Fourier transform operation realized with the fast Fourier transform (FFT) algorithm, and d is the propagation distance.

Equation (1) can be simplified by defining the Fourier transformation of the impulse response as $H(u,v;d)=FT\{h(x,y;d)\}$. Thus, the calculation of the propagated wavefield is simplified to

$$U_0(x,y;d) = FT^{-1}\{\hat{U}(u,v)\cdot H(u,v;d)\} \tag{2}$$

being $\hat{U}(u,v)$ the FT of $U(x,y)$ and (u,v) the spatial-frequency coordinates.

2.2. Calibration and quantitative phase imaging validation

The selection of the best defocus distance Δz is the key concept for retrieving high quality images. To properly select Δz, we have performed the following analysis using both amplitude (positive super high-resolution test target from Newport: https://www.newport.com/f/high-resolution-test-targets) and phase (quantitative phase target from Benchmark Technologies: https://www.benchmarktech.com/quantitativephasemicroscop) USAF-style resolution test targets: we have varied Δz by turning the vertical adjustment knob of the microscope in the range $-200\,\mu m < \Delta z < +500\,\mu m$ while using different vertical steps depending on the range, and the best image possible is retrieved by numerical processing for each Δz. The experimental methodology for every sample is as follows. First, we focus on the sample plane by introducing the sample in the microscope stage and vertically move it using the coarse/fine adjustment knob of the microscope. It is a regular procedure when using a bright-field intensity imaging mode but will not provide imaging conditions for phase samples. This will be our starting point ($\Delta z = 0\,\mu m$) from which positive/negative defocusing distances are produced using the fine adjustment vertical knob of the microscope. We are producing a different defocusing step depending on the defocusing range which as smaller as 10 µm for the range of interest. The results are summarized through Fig. 2 for both resolution test targets, where only a magnified image of the Group 9 is presented as image quality indicator. In addition, some plots along the horizontal lines of the 6 elements in Group 9 are also included to show how the elements are progressively lost as Δz is varied.

Through Fig. 2 we can see that the quality of the reconstructions (numerically propagated images) in terms of resolution is not symmetrical when considering positive or negative defocus distances. In general, negative distances destroy image quality faster than positive ones. Therefore, we have only included reconstructions until −200 µm. And not only image resolution is penalized but also global (qualitative) image quality is worse for $\Delta z < 0$ distances. So positive defocus distances seem to be much more suitable for our purpose. Thus, going to the positive side, we have realized that resolution stays stable (Group 9 – Element 6, from now on denoted as G9-E6) from approximately $\Delta z = 30\,\mu m$ to $\Delta z = 180\,\mu m$ and for both resolution test targets. As it can be seen on the plots corresponding with $\Delta z = 40$, 90, 120 and 160 µm, the 3 valleys (amplitude test) and peaks (phase test) corresponding with the G9-E6 are perfectly resolved while for higher and lower Δz distances, some elements in the Group 9 are not resolved. Thus, the proper defocusing range seems to be $30\,\mu m < \Delta z < 180\,\mu m$ at least taking into account the resolution limit as criterion.

To further narrow the defocusing range, we have computed the absolute standard deviation (SD) values at some clear areas in the background of the retrieved images as a function of Δz. Figure 3 plots the obtained results considering the SD values at three specific clear areas (marked with yellow rectangles) in the background of the amplitude (blue line) and phase (red line) images. Figure 3 also presents two illustrative cases of retrieved images for both resolution test targets at separated defocus distances ($\Delta z = 40\,\mu m$ and $\Delta z = 160\,\mu m$) to clearly identify the clear areas where SD is computed and the retrieved SD values. The values plotted in the central graphs

Optics EXPRESS

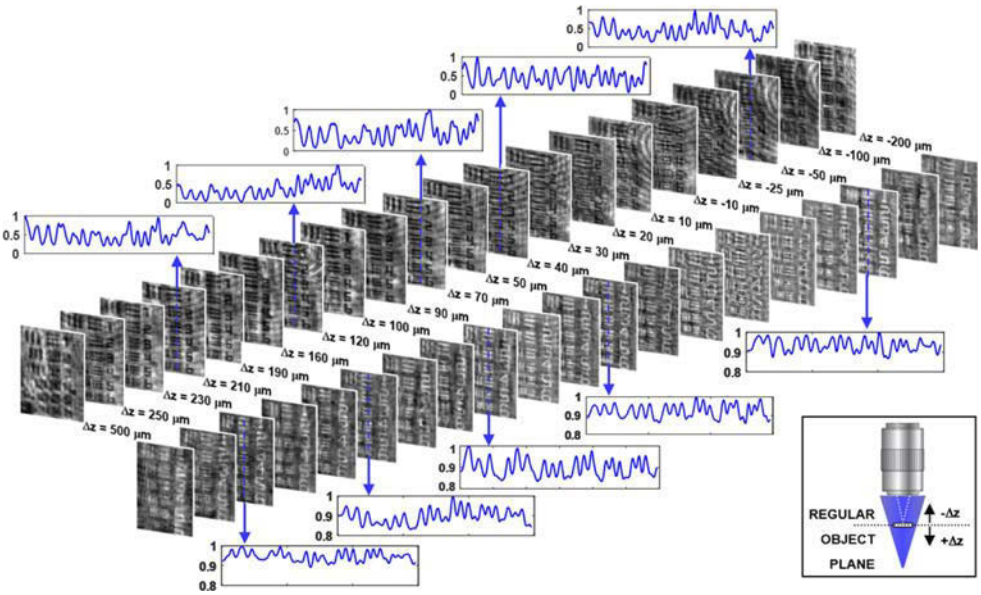

Fig. 2. Calibration procedure for selecting the best Δz distance considering amplitude (upper sequence of images) and phase (lower sequence of images) resolution test targets. The defocus distance varies from +500 to −200 μm and some representative images of the 6 Elements of the Group 9 are included in addition with some plots (normalized values) along the horizontal lines of the elements in the Group 9 for some selected distances.

corresponds with the averaged value coming from the 3 individual ones for each case. Since the plot for the amplitude test target presents strong variations, we have fitted a third-degree polynomial (black dashed line) in order to compute the crossing between the two curves. We can see that both curves are crossing from 90 to 100 μm, so we have selected 90 μm as ideal defocus distance for the experimental validation.

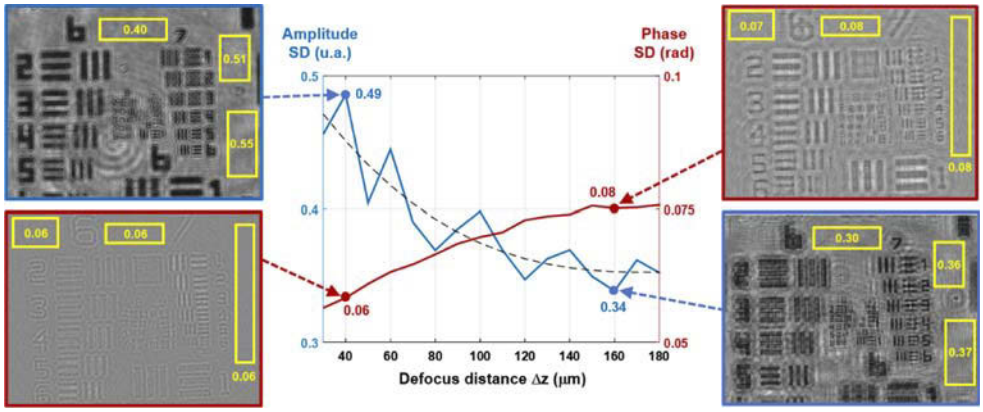

Fig. 3. Representation of the absolute SD (central graph) computed at clear background areas (yellow rectangles of the illustrative images) of the amplitude (blue plot) and phase (red plot) resolution test targets. The dashed black line corresponds to the third-degree polynomial fitting over the amplitude test case. The images represent the reconstructions for both targets when considering Δz = 40 μm (left images) and Δz = 160 μm (right images) and contain the computed values at the considered background areas.

Optics EXPRESS

Thus, Fig. 4 includes the full retrieved experimental results concerning both test targets and for $\Delta z = 90\,\mu m$. The (a) upper row shows the amplitude test case concerning (a.1) the direct intensity image provided by the microscope when imaging the input plane ($\Delta z = 0\,\mu m$) and (a.2) its central part magnified to clearly show the resolution limit, (a.3) the recorded digital in-line Gabor hologram, and (a.4) the retrieved intensity image after numerical propagation with (a.5) the magnification of its central area to be compared with (a.2). The (b) lower row presents a similar image sequence but for the phase resolution target case, showing retrieved phase images after numerical propagation. In general, we can say that, first, the numerical reconstructions are extremely reduced in noise in comparison with the direct image for both test targets since the spurious interference rings appearing in regular imaging conditions are strongly mitigated when defocusing is introduced. As consequence, image quality becomes improved in general. Maybe this is a casual issue depending on the specific system configuration (wavelength, objectives, coatings, etc.) but we think it is an improvement provided by the proposed methodology/system and should be noticed as well. Second, resolution limit is preserved (same last resolved element: G10-E1) when comparing (a.3) with (a.5) for the amplitude test case. Moreover, the same resolution limit (G10-E1) is also achieved for the phase test target (b.5). And finally but probably most important, phase image visualization is accessible (b.4)-(b.5) while it cannot be attained under regular imaging conditions (b.1)-(b.2).

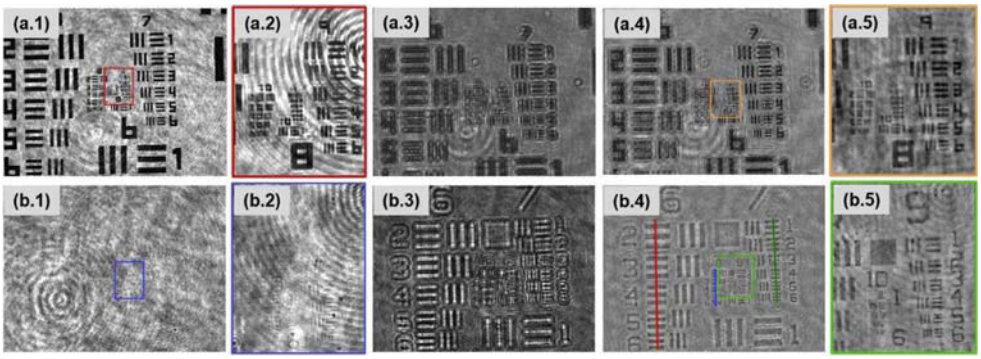

Fig. 4. Comparison results for both amplitude (upper row) and phase (lower row) test targets. Through the different columns: (1) presents the direct image under regular imaging conditions, (2) includes a magnification of the central area with the finest details of the tests, (3) shows the recorded in-line Gabor holograms, (4) depicts the reconstructed images – intensity in (a.4) and phase in (b.4) – after numerically refocusing of (3), and (5) magnifies the central area of (4).

Precisely, the retrieved phase distribution by numerical propagation allows QPI of the inspected sample. Figure 5 includes two types of quantitative results derived from the retrieved images of the phase resolution test case. On one hand, (a) the height of the phase target is computed from the retrieved phase step values ($\Delta\varphi$) through the equation:

$$\Delta t = \frac{\lambda\,\Delta\varphi}{2\pi(n_{test} - 1)} \tag{3}$$

where n_{test} is the refractive index value of the phase target material for the used illumination wavelength λ. The phase step is calculated from the plots along the RGB color-coded lines at Fig. 4(b.4) and corresponding with the groups 6, 7 and 8 of the phase test target. The obtained phase plots are included in Fig. 5(a), where we can clearly identify all the elements of each group (5 elements for G6 and G8, and 6 elements for G7). From those plots, the resulting phase step seems to be a little bit lower than 1 rad. Considering $\Delta\varphi = 0.85 \pm 0.1$ rad in average and taking

Optics EXPRESS

into account that the phase target material is Corning Eagle XG glass (n_{test} = 1.5185 for 450 nm according to https://refractiveindex.info/), the height of the phase target elements roughly equals to 117 ± 14 nm. This value is in good agreement with the value provided by the manufacturer (114.4 nm) which is based on mean values from measured targets coming from the same master substrate. And on the other hand, Fig. 5(b) includes the 3D visualization of the retrieved phase distribution for the central test elements showing 3D QPI capability.

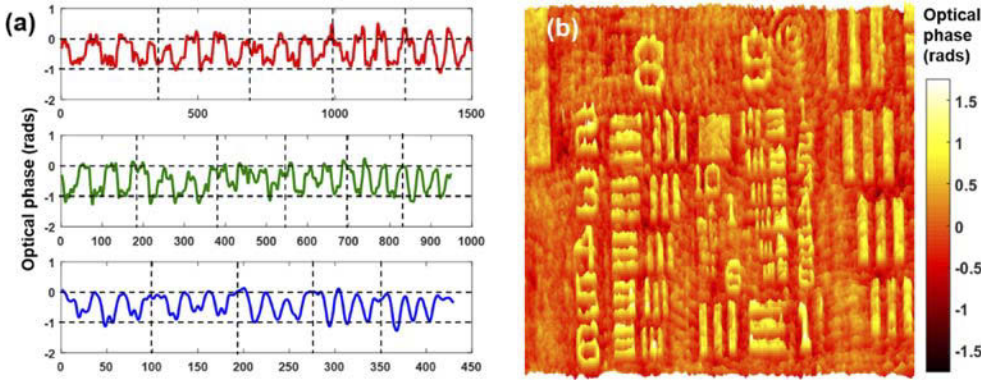

Fig. 5. QPI experimental results: (a) plots along the RGB color-coded lines of G6, G7 and G8 at Fig. 4(b.4) for calculation of the element height in the phase test target, and (b) 3D plot of the retrieved quantitative phase information.

3. Experimental validation outside resolution test targets

The proposed concept is now validated using different types of samples (not only resolution test targets) and considering $\Delta z = 90\,\mu m$. As for the calibration experiments, static samples experiments are obtained using the Mightex USB3.0 monochrome camera. Figure 6 presents the results when microbeads (Polybead Microspheres, 3 μm mean diameter) are imaged under regular imaging conditions [Fig. 6(a)] and with the proposed methodology [Fig. 6(b)]. The beads are on top of a microscope slide (air immersed) meaning that the refractive index step is maximum (not as when they are immersed in a given aqueous medium) and only a small cone of light is captured by the objective lens. Thus, only a small spherical cap of the bead can be reconstructed and, because of the bead's aberrations, the retrieved phase information becomes extremely noisy and plenty of vortices. For those reasons, the beads appear as a small spot of light surrounded by a dark ring, so phase imaging conditions are mainly ruled by noise and they are not included for the comparison. Nevertheless, Fig. 6 presents the results for the amplitude (intensity) distribution, showing comparable results between both imaging modalities.

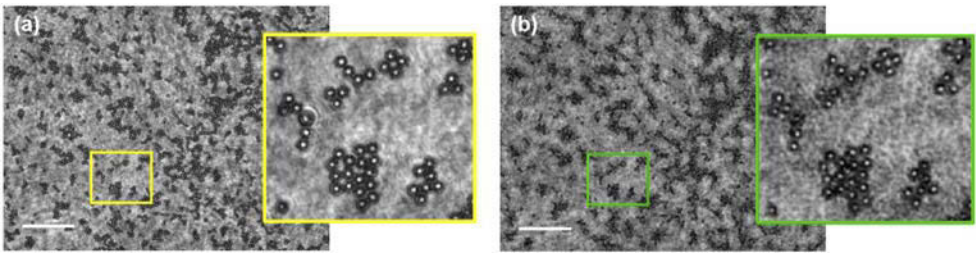

Fig. 6. Microbeads (3 μm in diameter) imaged under (a) regular conditions and (b) the proposed methodology. White scale bar on the left-down corner is 50 μm.

Optics EXPRESS

After intensity imaging capability validation, two different pure phase samples are considered. In the first case, a human cheek cell biosample (two different cells) is imaged and the results are included in Fig. 7. The cells are directly extracted using a clean cotton swab which is scraped inside the subject's mouth and then, smeared onto the microscope slide where a cover glass is added. In this case, no image is possible under regular imaging conditions [Figs. 7(a.1) and (b.1)] while they are visible using the proposed method under two-dimensional (2D) phase imaging modality [Figs. 7(a.2) and (b.2)] and 3D plot of the retrieved phase distributions including quantitative phase values [Figs. 7(a.3) and (b.3)]. The obtained results show the typical flat plateau containing some inner structures (granules and nucleus) of the cheek cells. However, there is a phase halo (positive in column 2 and negative in column 3) surrounding the cell border disturbing the reconstruction. This halo could be influenced by the twin image as well as from other issues in the recording scheme as consequence of the defocused recorded hologram.

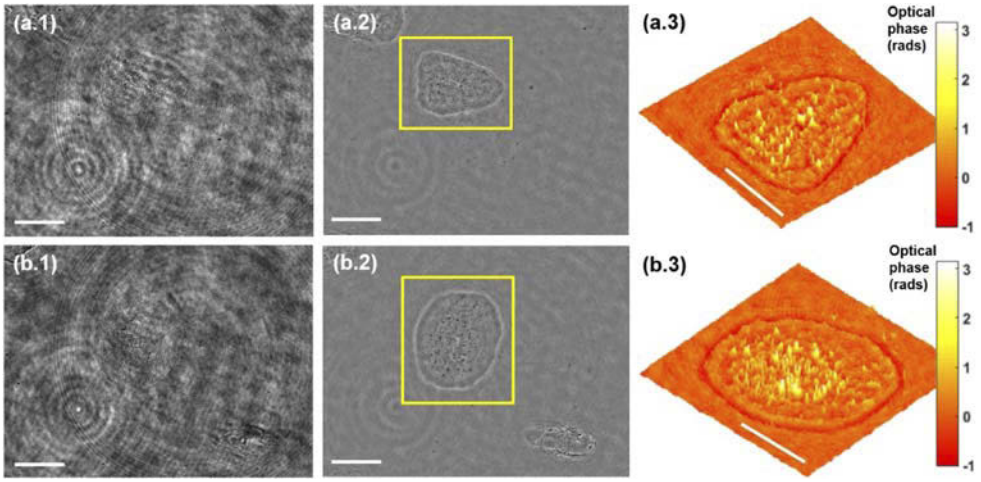

Fig. 7. Cheek cells imaged under (a.1)-(b.1) regular conditions and the proposed methodology using (a.2)-(b.2) retrieved phase distribution and (a.3)-(b.3) its 3D plot including quantitative values. White scale bar is 50 µm.

Finally, the second case involves a live human sperm sample. The sperm cells have approximately a head's length and width of 4 and 5 µm, respectively, a total length of 45 µm and a tail's width below 1 µm. The sample is placed in a regular microscope slide with a coverslip allowing the swimming of the cells at different heights. No pre-filtering nor pre-preparation (centrifugation, dilution, re-suspension, etc.) is applied, so the sample contains a lot of additional seminal particles. Due to the fast movement of the sperm cells, we have replaced the previous camera (Mightex SMN-B050-U) by a faster one (Ximea USB3.0 MQ042MG-CM, CMOS sensor type, 2048×2048 pixels, 5.5×5.5 µm pixel pitch) at 90 fps. To provide a similar FOV than for the static images, we have selected a frame size of 1024×768 pixels and the total recording time is 2 seconds.

Figure 8 presents the first frames of the obtained movies where the recorded hologram (Visualization 1) and the pre-filtered hologram removing all static stuff and enhancing cell's movement for image processing (Visualization 2) are presented in (a) and (b), respectively. The rest of the images at Fig. 8 contains different visualization modes coming from the retrieval of the complex amplitude information allowed by holography. Moreover, since there are cells swimming at different depths in the sample, we can numerically focus to every single plane to perfectly see each sperm cell in focus. In particular, the video sequence presented in Fig. 8 contains two different movement planes, the first one including 4 spermatozoa while only 1 in

Optics EXPRESS

the second one. Thus, Figs. 8(c.1) and (c.2) present the visualizations considering DIC imaging modality (one pixel of lateral shift) in horizontal (Visualization 3) and vertical (Visualization 4), respectively, each one corresponding to a different focusing plane. Figures 8(d.1)-(d.2) include the positive 2D (Visualization 5) and 3D (Visualization 6), respectively, quantitative phase contrast visualizations for the first plane, and Figs. 8(e.1)-(e.2) shows the negative 2D (Visualization 7) and 3D (Visualization 8), respectively, quantitative phase contrast visualizations for the second plane.

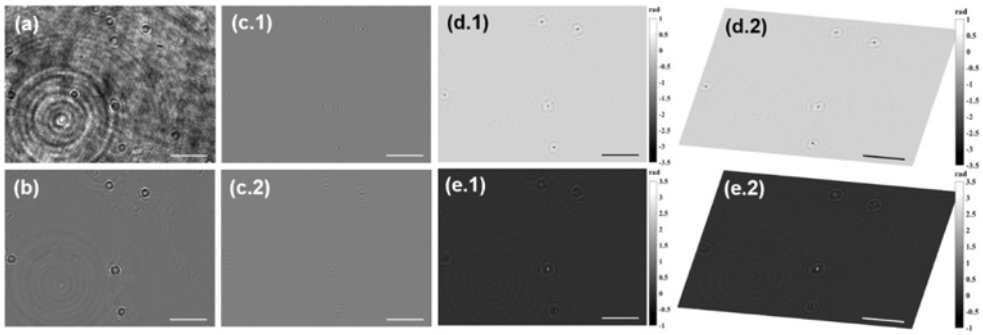

Fig. 8. Live human sperm cells in free movement. First frames of a 2 seconds video movies showing: (a) recorded hologram (Visualization 1), (b) pre-filtered hologram (Visualization 2), (c-1)-(c.2) DIC in horizontal (Visualization 3) and vertical (Visualization 4) for the two focusing planes, (d.1)-(d.2) 2D (Visualization 5) and 3D (Visualization 6) quantitative positive phase contrast images for the first focusing plane, and (e.1)-(e.2) 2D (Visualization 7) and 3D (Visualization 8) quantitative negative phase contrast images for the second focusing plane. Scale bars in all images are 50 µm and lateral gray color bar at images (d.1), (d.2), (e.1) and (e.2) represents optical phase in rad.

4. Discussion and conclusions

Through this manuscript, we have presented, calibrated and experimentally validated an extremely simple way to convert a regular bright-field microscope into a holographic microscope for QPI. As we have stated at the introduction, the possibility to provide coherent sensing capabilities to a regular microscope is nowadays very interesting issue because it expands the use of regular microscopes for the analysis of biosamples without the need to manipulate (staining, fixing, damaging, etc.) them. In that sense, a lot of contributions were previously reported to update a regular microscope into a coherence sensing microscope by adding external modules to the output port or by making some simple changes in the microscope embodiment. This contribution has probably presented the easiest way to allow holographic imaging using an upright commercially available microscope by i) only adding a coherent illumination source, ii) defocusing the recorded image and iii) implementing some non-complex digital image processing routines.

Regarding the illumination source, we have used here a fiber-coupled laser diode but cheaper laser sources such as, for instance, a DVD laser diode [55] or even LED light [56], can be used thus defining an extremely cost-effective solution. Concerning the suitable defocus distance, we have applied a criterion based on SD analysis for fine selection of the proper Δz distance. Although other criteria based on optimization of other metrics (more complex models for noise analysis) can be applied, the one used here is simple and provides an output in the middle of the initially selected range ($30 < \Delta z < 180$ µm) when resolution limit is analyzed. However, it is not critical that the defocus distance will not be exactly 90 microns since image quality is qualitatively maintained in a wide defocus distance range thus allowing to refocus the sperm cells flowing at different depths in the chamber with a similar image quality. We have here included

Optics EXPRESS

the case of a 20X 0.46NA objective and the procedure for properly selection of the best defocus distance. For other microscope lenses, the proper defocus distances will change as the lens magnification factor also changes. But similar strategy (that only needs to be done once) can be followed to define the proper defocus distance for every objective. So no additional complexity will be added when expanding the proposed method to other microscope lenses. And finally, numerical processing is nowadays something inherent to many digital image formation in order to achieve the best image quality possible. In this case, we are implementing simple numerical routines for computing lensfree propagation, something available for long time ago that does not add additional difficulties.

The calibration analysis performed in the system allows to validate resolving power in the proposed methodology. Normally, resolution limit (R) in coherent light microscopy can be computed as proportional to the ratio between illumination wavelength and numerical aperture in the form of $R = k\lambda/NA$, being k the constant of proportionality that equals to 0.82 for imaging systems based on circular apertures [57]. In our case, $R = 0.8\,\mu m$ for the used illumination wavelength and NA lens. However, the object's spectrum is not abruptly truncated by the circular limiting aperture as in conventional imaging systems because the object is defocused. As consequence, vignetting must appear close to the aperture borders at the Fourier domain meaning a progressive limitation of the object's high spatial frequency content. This fact will probably introduce a small lost in the resolution limit. In the calibration procedure, we have measured a resolution limit of 0.976 μm coming from G10-E1 as last resolved element on both test targets (note that G10-E2 corresponding with 0.87 μm is not resolved). So the experimental resolution limit perfectly matches with the theoretically predicted value.

From the retrieved quantitative phase images, we can observe coherent noise (interference patterns coming from back reflections, coherent artefacts, non-uniformities, etc.) introducing phase disturbances in the retrieved QPI values. It is a direct consequence of using coherent illumination provided by the laser diode source. All this generated coherent noise can be strongly mitigated by using, for instance, partially coherent illumination [58], thus reducing and improving performance of the proposed method concerning QPI. Moreover, although it is not the case here, additional image processing algorithms can be conducted at the retrieved image for further increase its final quality in terms of twin image minimization [58]. Additionally, the proposed methodology seems to be incompatible in its actual form with other intensity imaging modalities such as bright-field or fluorescence because the sample is moved away from the conventional input plane, so no direct image is allowed on the camera. Thus, multimodal imaging capabilities (as previously identified) are prevented and the only solution comes from duplicating the digital sensor in order to capture in parallel the different imaging modalities. All those drawbacks open new possibilities for circumventing them in future developments.

But maybe the main limitation of the proposed method concerns to the Gabor restriction of the imaged samples, that is, the sample must be a weak diffractive one meaning that the amount of light blocked/diffracted by the sample should be a small fraction of the one passing without being perturbed by the sample. Otherwise, holographic imaging is not allowed and diffraction dominates the process, preventing the accurate recovery of the complex wavefront diffracted by the sample, so other methodologies must be implemented to retrieve complex amplitude distribution [59]. However, there is a wide range of biological samples (single cell analysis, thin structured samples, sparse biosamples, etc.) fulfilling the Gabor's condition and so, they are perfectly suitable to be imaged under the proposed methodology.

In summary, we have presented probably the easiest way to convert a standard bright field microscope into a holographic one by considering only 3 minimum modifications: replacement of the broadband illumination source by a coherent one (a laser diode in the proposed manuscript), defocusing of the object plane to allow the recording of a digital in-line Gabor hologram (90 μm for the used 20X objective lens) and proper numerical propagation tools to refocus the

Optics EXPRESS

sample image (digital implementation of the free space propagation integral). Using these 3 modifications, different types of samples have been used to experimentally validate the proposed concept: resolution test targets (amplitude and phase ones) to provide calibration and QPI validation as well as microbeads and phase biosamples (cheek and sperm cells) to show the potential of the proposed method. Different imaging visualization modes including QPI plots have been reported thus validating coherent sensing capabilities in a regular microscope embodiment.

Funding. Grant PID2020-120056GB-C21 funded by MCIN/AEI/10.13039/501100011033.

Disclosures. The authors declare that there are no conflicts of interest related to this article.

Data availability. Data underlying the results presented in this paper are not publicly available at this time but may be obtained from the authors upon reasonable request.

References

1. M. K. Kim, *Digital Holographic Microscopy: Principles, Techniques, and Applications* (Springer, 2011).
2. N. T. Shaked, Z. Zalevsky, and L. L. Satterwhite, *Biomedical Optical Phase Microscopy and Nanoscopy* (Oxford Academy, 2012).
3. B. Bhaduri, C. Edwards, H. Pham, R. Zhou, T. H. Nguyen, L. L. Goddard, and G. Popescu, "Diffraction phase microscopy: principles and applications in materials and life sciences," Adv. Opt. Photonics **6**(1), 57–119 (2014).
4. N. T. Shaked, V. Micó, M. Trusiak, A. Kuś, and S. K. Mirsky, "Off-axis digital holographic multiplexing for rapid wavefront acquisition and processing," Adv. Opt. Photonics **12**(3), 556–611 (2020).
5. T. Kreis, "Application of digital holography for nondestructive testing and metrology: a review," IEEE Trans. Ind. Inf. **12**(1), 240–247 (2016).
6. Y. Emery, T. Colomb, and E. Cuche, "Metrology applications using off-axis digital holography microscopy," JPhys Photonics **3**(3), 034016 (2021).
7. M. K. Kim, "Principles and techniques of digital holographic microscopy," J. Photonics Energy **1**(1), 018005 (2010).
8. T. Zhang and I. Yamaguchi, "Three-dimensional microscopy with phase-shifting digital holography," Opt. Lett. **23**(15), 1221–1223 (1998).
9. F. Dubois, L. Joannes, and J.-C. Legros, "Improved three-dimensional imaging with a digital holography microscope with a source of partial spatial coherence," Appl. Opt. **38**(34), 7085–7094 (1999).
10. H. Iwai, C. Fang-Yen, G. Popescu, A. Wax, K. Badizadegan, R. R. Dasari, and M. S. Feld, "Quantitative phase imaging using actively stabilized phase-shifting low-coherence interferometry," Opt. Lett. **29**(20), 2399–2401 (2004).
11. D. M. Gale, M. I. Pether, and J. C. Dainty, "Linnik microscope imaging of integrated circuit structures," Appl. Opt. **35**(1), 131–148 (1996).
12. G. S. Kino and S. C. Chim, "Mirau correlation microscope," Appl. Opt. **29**(26), 3775–3783 (1990).
13. S. Reichelt and H. Zappe, "Combined Twyman-Green and Mach-Zehnder interferometer for microlens testing," Appl. Opt. **44**(27), 5786–5792 (2005).
14. S. Mahajan, V. Trivedi, P. Vora, V. Chhaniwal, B. Javidi, and A. Anand, "Highly stable digital holographic microscope using Sagnac interferometer," Opt. Lett. **40**(16), 3743–3746 (2015).
15. J. Zheng, P. Gao, and X. Shao, "Opposite-view digital holographic microscopy with autofocusing capability," Sci. Rep. **7**(1), 4255 (2017).
16. V. Chhaniwal, A. S. G. Singh, R. A. Leitgeb, B. Javidi, and A. Anand, "Quantitative phase-contrast imaging with compact digital holographic microscope employing Lloyd's mirror," Opt. Lett. **37**(24), 5127–5129 (2012).
17. G. Popescu, T. Ikeda, R. R. Dasari, and M. S. Feld, "Diffraction phase microscopy for quantifying cell structure and dynamics," Opt. Lett. **31**(6), 775–777 (2006).
18. V. Mico, C. Ferreira, Z. Zalevsky, and J. García, "Spatially-multiplexed interferometric microscopy (SMIM): converting a standard microscope into a holographic one," Opt. Express **22**(12), 14929–14943 (2014).
19. JÁ Picazo-Bueno and V. Micó, "Opposed-view spatially multiplexed interferometric microscopy," J. Opt. **21**(3), 035701 (2019).
20. G. Popescu, *Quantitative Phase Imaging of Cells and Tissues* (McGraw-Hill, NY, 2011).
21. K. Lee, K. Kim, J. Jung, J. Heo, S. Cho, S. Lee, G. Chang, Y. J. Jo, H. Park, and Y. K. Park, "Quantitative Phase Imaging Techniques for the Study of Cell Pathophysiology: From Principles to Applications," Sensors **13**(4), 4170–4191 (2013).
22. Y. K. Park, C. Depeursinge, and G. Popescu, "Quantitative phase imaging in biomedicine," Nat. Photonics **12**(10), 578–589 (2018).
23. J. Di, Y. Li, M. Xie, J. Zhang, C. Ma, T. Xi, E. Li, and J. Zhao, "Dual-wavelength common-path digital holographic microscopy for quantitative phase imaging based on lateral shearing interferometry," Appl. Opt. **55**(26), 7287–7293 (2016).
24. T. Sun, Z. Zhuo, W. Zhang, J. Lu, and P. Lu, "Single-shot interference microscopy using a wedged glass plate for quantitative phase imaging of biological cells," Laser Phys. **28**(12), 125601 (2018).
25. JÁ Picazo-Bueno, M. Trusiak, J. García, and V. Micó, "Spatially multiplexed interferometric microscopy: principles and applications to biomedical imaging," JPhys Photonics **3**(3), 034005 (2021).

Optics EXPRESS

26. JÁ Picazo-Bueno, J. García, and V. Micó, "Single-element reflective digital holographic microscopy," Front. Phys. **9**, 639607 (2021).
27. M. Trusiak, J. A. Picazo-Bueno, K. Patorski, P. Zdankowski, and V. Micó, "Single-shot two-frame π-shifted spatially multiplexed interference phase microscopy," J. Biomed. Opt. **24**(09), 1 (2019).
28. S. Ebrahimi, M. Dashtdar, E. Sánchez-Ortiga, M. Martínez-Corral, and B. Javidi, "Stable and simple quantitative phase-contrast imaging by Fresnel biprism," Appl. Phys. Lett. **112**(11), 113701 (2018).
29. P. Bon, G. Maucort, B. Wattellier, and S. Monneret, "Quadriwave lateral shearing interferometry for quantitative phase microscopy of living cells," Opt. Express **17**(15), 13080–13094 (2009).
30. G. J. Tearney and C. Yang, "Wavefront image sensor chip," Opt. Express **18**(16), 16685–16701 (2010).
31. B. Kemper, A. Vollmer, C. E. Rommel, J. Schnekenburger, and G. von Bally, "Simplified approach for quantitative digital holographic phase contrast imaging of living cells," J. Biomed. Opt. **16**(2), 026014 (2011).
32. N. T. Shaked, "Quantitative phase microscopy of biological samples using a portable interferometer," Opt. Lett. **37**(11), 2016–2018 (2012).
33. D. Roitshtain, N. A. Turko, B. Javidi, and N. T. Shaked, "Flipping interferometry and its application for quantitative phase microscopy in a micro-channel," Opt. Lett. **41**(10), 2354–2357 (2016).
34. K. Lee and Y. Park, "Quantitative phase imaging unit," Opt. Lett. **39**(12), 3630–3633 (2014).
35. J. Di, Y. Li, K. Wang, and J. Zhao, "Quantitative and Dynamic Phase Imaging of Biological Cells by the Use of the Digital Holographic Microscopy Based on a Beam Displacer Unit," IEEE Photonics J. **10**(4), 1–10 (2018).
36. R. Guo, S. K. Mirsky, I. Barnea, M. Dudaie, and N. T. Shaked, "Quantitative phase imaging by wide-field interferometry with variable shearing distance uncoupled from the off-axis angle," Opt. Express **28**(4), 5617–5628 (2020).
37. J. Frank, J. Matrisch, J. Horstmann, S. Altmeyer, and G. Wernicke, "Refractive index determination of transparent samples by noniterative phase retrieval," Appl. Opt. **50**(4), 427–433 (2011).
38. Y. Li, J. Di, C. Ma, J. Zhang, J. Zhong, K. Wang, T. Xi, and J. Zhao, "Quantitative phase microscopy for cellular dynamics based on transport of intensity equation," Opt. Express **26**(1), 586–593 (2018).
39. J. Á. Picazo-Bueno and V. Micó, "Optical module for single-shot quantitative phase imaging based on transport of intensity equation with field of view multiplexing," accepted for publication in Opt. Express.
40. JÁ Picazo-Bueno, M. Trusiak, and V. Micó, "Single-shot slightly off-axis digital holographic microscopy with add-on module based on beamsplitter cube," Opt. Express **27**(4), 5655–5669 (2019).
41. M. Trusiak, M. Cywińska, V. Micó, JÁ Picazo-Bueno, C. Zuo, P. Zdańkowski, and K. Patorski, "Variational Hilbert quantitative phase imaging," Sci. Rep. **10**(1), 13955 (2020).
42. D. Gabor, "A new microscopic principle," Nature **161**(4098), 777–778 (1948).
43. G. L. Rogers, "Experiments in diffraction microscopy," Proc. - R. Soc. Edinburgh, Sect. A: Math. Phys. Sci. **63**(3), 193–221 (1952).
44. V. Micó, J. García, Z. Zalevsky, and B. Javidi, "Phase-Shifting Gabor Holographic Microscopy," J. Display Technol. **6**(10), 484–489 (2010).
45. T. Kreis, *Handbook of Holographic Interferometry: Optical and Digital Methods*. Wiley-VCH Verlag, Weinheim, Germany, 2005.
46. J. Sheng, E. Malkiel, and J. Katz, "Digital holographic microscope for measuring three-dimensional particle distributions and motions," Appl. Opt. **45**(16), 3893–3901 (2006).
47. S.-H. Lee, Y. Roichman, G.-R. Yi, S.-H. Kim, S.-M. Yang, A. van Blaaderen, P. van Oostrum, and D. G. Grier, "Characterizing and tracking single colloidal particles with video holographic microscopy," Opt. Express **15**(26), 18275–18282 (2007).
48. X. Wu, G. Gréhan, S. Meunier-Guttin-Cluzel, L. Chen, and K. Cen, "Sizing of particles smaller than 5 μm in digital holographic microscopy," Opt. Lett. **34**(6), 857–859 (2009).
49. Y.-S. Choi and S.-J. Lee, "High-accuracy three-dimensional position measurement of tens of micrometers size transparent microspheres using digital in-line holographic microscopy," Opt. Lett. **36**(21), 4167–4169 (2011).
50. J. P. Ryle, S. McDonnell, B. Glennon, and J. T. Sheridan, "Calibration of a digital in-line holographic microscopy system: depth of focus and bioprocess analysis," Appl. Opt. **52**(7), C78–C87 (2013).
51. Y. Zagzag, M. F. Soddu, A. D. Hollingsworth, and D. G. Grier, "Holographic molecular binding assays," Sci. Rep. **10**(1), 1932 (2020).
52. F. Dubois, C. Schockaert, N. Callens, and C. Yourassowsky, "Focus plane detection criteria in digital holography microscopy by amplitude analysis," Opt. Express **14**(13), 5895–5908 (2006).
53. M. Antkowiak, N. Callens, C. Yourassowsky, and F. Dubois, "Extended focused imaging of a microparticle field with digital holographic microscopy," Opt. Lett. **33**(14), 1626–1628 (2008).
54. F. Dubois, A. El Mallahi, J. Dohet-Eraly, and C. Yourassowsky, "Refocus criterion for both phase and amplitude objects in digital holographic microscopy," Opt. Lett. **39**(15), 4286–4289 (2014).
55. JÁ Picazo-Bueno, Z. Zalevsky, J. García, and V. Micó, "Superresolved spatially multiplexed interferometric microscopy," Opt. Lett. **42**(5), 927–930 (2017).
56. R. Guo, B. Yao, P. Gao, J. Min, M. Zhou, J. Han, X. Yu, X. Yu, M. Lei, S. Yan, Y. Yang, D. Dan, and T. Ye, "Off-axis digital holographic microscopy with LED illumination based on polarization filtering," Appl. Opt. **52**(34), 8233–8238 (2013).

Optics EXPRESS

57. V. Micó, J. Zheng, J. Garcia, Z. Zalevsky, and P. Gao, "Resolution enhancement in quantitative phase microscopy," Adv. Opt. Photonics **11**(1), 135–214 (2019).
58. B. Perucho and V. Micó, "Wavefront holoscopy: application of digital in-line holography for the inspection of engraved marks in progressive addition lenses," J. Biomed. Opt. **19**(1), 016017 (2014).
59. V. Micó, J. García, Z. Zalevsky, and B. Javidi, "Phase-shifting Gabor holography," Opt. Lett. **34**(10), 1492–1494 (2009).